AIAA 79-0770R

Refined Prediction Method for Supersonic Nonsteady Aerodynamics with AIC Partition Scheme

Jack Morito Ii*
The Boeing Company, Seattle, Wash.

This paper describes a study of the causes of the inaccuracies in the evaluation of airloads by application of the Mach box numerical scheme. A refinement to lessen inaccuracies in the evaluation of steady/unsteady supersonic airloads is presented. The refinement is based on the aerodynamic influence coefficient (AIC) partition scheme and application of conical flow concept in the small perturbation flowfield. The refinement is intended to minimize the nonconverging error due to irregular points. Care is taken to retain the computational efficiency of the basic Mach box scheme. The new method is demonstrated for both planar and nonplanar interaction cases and is shown to result in smoother, more realistic pressure distributions.

Nomenclature

a = speed of sound $= U/M$
$A(n,m)$ = integration area of box n,m
b_l = chordwise dimension of Mach box
$C_{\bar{\nu}\bar{\mu}\bar{\lambda}}$ = spatial AIC for velocity potential
$C_{\bar{\nu}\bar{\mu}_0}, C_{\bar{\nu}\bar{\mu}}$ = planar AIC for velocity potential
$\Delta C_{pj}^{n,m}$ = pressure coefficient difference at box n,m for the jth mode
$f_j(x,y)$ = jth mode shape deflection at (x,y)
k_s, k_l = reduced frequencies based on $s, = s\omega/U$, and on $b_l, = b_l\omega/U$, respectively
$\bar{k}_l$ = nondimensional number $= k_l M^2/\beta^2$
M = Mach number $= U/a$
n_c, m_c, l_c = sending surface coordinate system
$\bar{n}_c, \bar{m}_c, \bar{l}_c$ = receiving point coordinate system
$\Delta P(x,y,t)$ = pressure difference between upper and lower surface at (x,y) and at time t
Q_{ij} = generalized force due to the deformation in the ith elastic mode and loading for the jth mode deflections
q = dynamic pressure of the freestream
$q_j(t)$ = generalized coordinate relating physical deflection to jth modal deflections

$$z(x,y,t) = \sum_j f_j(x,y) q_j(t)$$

s = wing semispan
t = time
U = freestream velocity
$WW(\nu,\mu)$ = area of wing portion of leading-edge wing box (ν,μ)
$WD(\nu,\mu)$ = area of diaphragm portion of leading-edge wing box (ν,μ)
$DD(\nu,\mu)$ = area of diaphragm portion of leading-edge diaphragm box (ν,μ)
$DW(\nu,\mu)$ = area of wing portion of leading-edge wing box (ν,μ)
u,v,w = perturbation velocities
x,y,z = coordinate system in general
X_W, Y_W, Z_W = wing local coordinate system
X_T, Y_T, Z_T = tail local coordinate system
$\alpha^{n,m}$ = edge box area ratio for box n,m
β = $(M^2-1)^{1/2}$
$\bar{\nu},\bar{\mu},\bar{\lambda}$ = $\bar{n}_c, \bar{m}_c, \bar{l}_c$ coordinate location of a pulse sending box
ξ,η,ζ = dummy variables of integration in $\bar{n}_c, \bar{m}_c, \bar{l}_c$ coordinate system
$\phi(x,y,t)$ = perturbated velocity potential at (x,y) and at time t
ω = circular frequency

Subscripts

L = lower limit of integration; left-hand surface; lower surface
R = right-hand surface
T = tail
U = upper surface
W = wing
i = ith segment of the leading edge
0 = nontime dependent part

Superscripts

$(n,m)\ (\nu,\mu)$ = box location
$(\ )$ = amplitude and average value weighted by area

Introduction

THE numerical evaluation of linearized aerodynamic loadings in unsteady supersonic inviscid flow is most effectively achieved in the low-to-moderate supersonic range by using the aerodynamic influence coefficient (AIC) method of lifting surface theory, first proposed by Pines et al.[1] and Zartarian.[2,3] This AIC method of applying the numerical box scheme, however, may produce highly inaccurate chordwise and spanwise pressure fluctuations, even though its performance on some generalized force computation is acceptable. Earlier estimation that accuracy could be improved by use of a finer box grid is in error because the pressure fluctuations merely increase in spatial frequency, but do not decrease in amplitude.

Various schemes have been attempted to reduce the inaccurate pressure fluctuations. These are a simple upwash weighted technique with a smoothing scheme to the velocity potential distribution by Andrew and Moore,[4] characteristic box method by Zartarian[5] and Stark,[6] subdivision method by Ii,[7] and weighted upwash method by Chipman.[8] Some of these schemes, however, are inefficient in computation and others have not been proved theoretically correct. There is also a question about their convergence.

Presented as Paper 79-0770 at the AIAA/ASME/ASCE/AHS 20th Structures, Structural Dynamics and Materials Conference, St. Louis, Mo., April 4-6, 1979; submitted July 16, 1979; revision received Aug. 13, 1980.

*Research Specialist. Member AIAA.

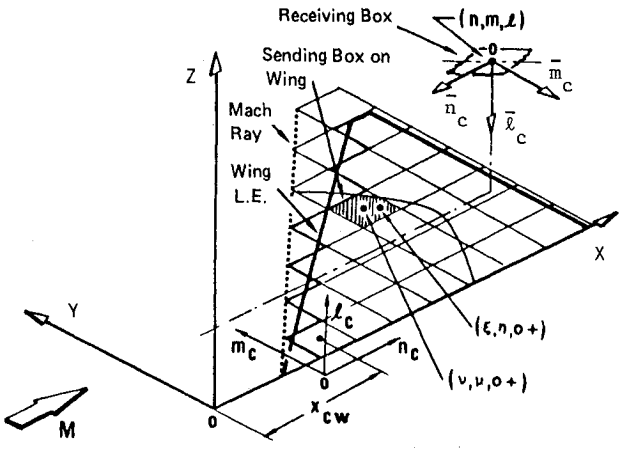

Fig. 1 Receiving point coordinate system.

In this paper, the cause of the fluctuations is studied and a remedy derived. In particular, it is shown that the irregular jaggedness of the artificial leading edges formed by the box pattern leads to a nonconverging error. By correctly weighting the integrations performed along these critical planform edge regions, the present method is much improved. The AICs over the critical leading-edge boxes are exactly computed over both the wing and diaphragm elements for $k=0$ and numerically computed for $k\neq 0$. However, to obtain further improvement, it is found necessary to use additional revised values of normal wash in the diaphragm regions by applying the conical flow concept as first suggested by Stark.[6] This combination of improvements is demonstrated to result in significantly better accuracy in both planar and nonplanar cases.

Both planar and nonplanar numerical results obtained through both refined and conventional techniques are compared with the exact solution for $k=0$ and are also presented for cases where $k\neq 0$.

Thin-Airfoil Theory in Supersonic Flow

Thin-airfoil or small-perturbation theory is applied to describe the flow patterns that result when small disturbances are superposed on parallel uniform flow. When coordinate axes are fixed on a thin body placed in uniform flow, the perturbation velocity potential satisfies the differential equation,

$$(1-M^2)\phi_{xx}+\phi_{yy}+\phi_{zz}=(2M/a)\phi_{xt}+(1/a^2)\phi_{tt} \tag{1}$$

If the time variation of the pulsing source singularity is harmonic, the solution results in an integral expression for $\phi(x,y,z;t)$ which is dependent upon the distribution of sources and the location of the point (x,y,z) and time t, that is[9,10,11]

$$\phi(x,y,z;t)=-e^{i\omega t}/\pi\int_0^{x-\beta z}\mathrm{d}\xi\int_{y-\eta_0}^{y+\eta_0}$$
$$\times W_0(\xi,\eta,0+)\,e^{-i\omega M(x-\xi)/a\beta^2}\cos\omega R_h/a\beta^2\,\mathrm{d}\eta \tag{2}$$

For a planform with a supersonic leading edge, the integration area is a portion of the planform that lies inside the forward Mach cone emanating from (x,y,z); $0+$ indicates the upper surface of the pulse-sending box, and

$$R_h=[(x-\xi)^2-\beta^2\{(y-\eta)^2+z^2\}]^{1/2}=\text{hyperbolic radius}$$

If the planform has a subsonic leading, trailing, or streamwise edge at its tip, "diaphragms" are introduced using the "Evvard concept."[12] The source distribution that is placed on the diaphragm is initially unknown, and is evaluated using the boundary condition $\Delta p=0$ at all points not on the wing surface.

Numerical Computation in the Mach Box Grid System

If the integration area may be split into sufficiently small elementary areas, one may make an approximation in the evaluation of the double integral equation (2).

In order to establish a convenient counting system for the grid of sending boxes a transformation is made from the dimensional coordinate system to a nondimensional one (n_c,m_c,l_c) in which the sending boxes are located at $(\nu,\mu,0)$, where ν and μ are integers. This transformation with the wing as sending surface is,

$$\begin{aligned} n_c&=(X_W-X_{CW})/b_1+1\\ m_c&=\beta Y_W/b_1+\tfrac{1}{2}\\ l_c&=\beta Z_W/b_1 \end{aligned} \tag{3}$$

where X_{CW} is the location of the first box center on the sending surface. A similar transformation is used when the tail is the sending surface, with X_W,Y_W,Z_W,X_{CW}, replaced by X_T,Y_T,Z_T,X_{CT}, respectively.

A final transformation which is

$$\begin{aligned} \bar{n}_c&=-(n_c-n)\\ \bar{m}_c&=-(m_c-m)\\ \bar{l}_c&=-(l_c-l) \end{aligned} \tag{4}$$

establishes a nondimensional coordinate system centered on the receiving point, see Fig. 1. The location of a sending box is $(\bar{\nu},\bar{\mu},\bar{\lambda})$ in this receiving coordinate system.

The expression for the perturbation velocity potential of Eq. (2) may now be expressed as

$$\phi_0(0,0,0)=\sum_{\bar{\nu}}\sum_{\bar{\mu}} w_{0\nu\mu}C_{\bar{\nu}\bar{\mu}\bar{\lambda}} \tag{5}$$

where

$$C_{\bar{\nu}\bar{\mu}\bar{\lambda}}=-\frac{1}{\pi}\int_{\bar{\xi}_L}^{\bar{\xi}_U}\int_{\bar{\eta}_L}^{\bar{\eta}_U}\frac{e^{-i\bar{k}_1\xi}\cos[(\bar{k}_1/M)\sqrt{\bar{\xi}^2-\bar{\eta}^2-\bar{\lambda}^2}]}{\sqrt{\bar{\xi}^2-\bar{\eta}^2-\bar{\lambda}^2}}\,\mathrm{d}\bar{\xi}\mathrm{d}\bar{\eta} \tag{6}$$

and is known as an aerodynamic influence coefficient or AIC.

Three more forms of AICs are required for the three-dimensional analysis. They are the AICs associated with the upwash $W_{\bar{\nu}\bar{\mu}\bar{\lambda}}$, sidewash $V_{\bar{\nu}\bar{\mu}\bar{\lambda}}$, and the longitudinal wash $U_{\bar{\nu}\bar{\mu}\bar{\lambda}}$.

Since the integrand of $C_{\bar{\nu}\bar{\mu}\bar{\lambda}}$ in Eq. (6) becomes singular at the Mach hyperbola, some manipulation of $C_{\bar{\nu}\bar{\mu}\bar{\lambda}}$ is needed to render it amenable to numerical integration. To this end, the function $G(\bar{\nu},\bar{\mu},\bar{\lambda})$ is introduced, where

$$G(\bar{\xi},\bar{\eta},\bar{\lambda})=\frac{\cos[\bar{k}_1/M(\bar{\xi}^2-\bar{\eta}^2-\bar{\lambda}^2)^{1/2}]}{(\bar{\xi}^2-\bar{\eta}^2-\bar{\lambda}^2)^{1/2}}=\frac{\partial}{\partial\bar{\xi}}F(\tau,\bar{\eta}) \tag{7}$$

where F is the Bessel function series expressed by

$$F(\tau,\bar{\eta})=J_0(k_1\tau/M)\theta+\sum_{r=1}^{\infty}\frac{(-1)^r}{r}J_{2r}(\bar{k}_1\tau/M)\sin(2r\theta) \tag{8}$$

where

$$\tau=(\bar{\xi}^2-\bar{\lambda}^2)^{1/2}\geq 0$$

and

$$\theta=\sin^{-1}\bar{\eta}/\tau$$

Substitution of Eqs. (7) and (8) into Eq. (6) yields

$$C_{\bar{\nu}\bar{\mu}\bar{\lambda}}=-\frac{1}{\pi}\int_{\bar{\xi}_L}^{\bar{\xi}_U}e^{-i\bar{k}_1\xi}[F(\tau,\bar{\eta}_U)-F(\tau,\bar{\eta}_L)]\,\mathrm{d}\bar{\xi} \tag{9}$$

$C_{\bar{\nu}\bar{\mu}\bar{\lambda}}$ can be evaluated from this expression using numerical integration technique, since F is closely approximated by the first few terms of the infinite summation in Eq. (8).

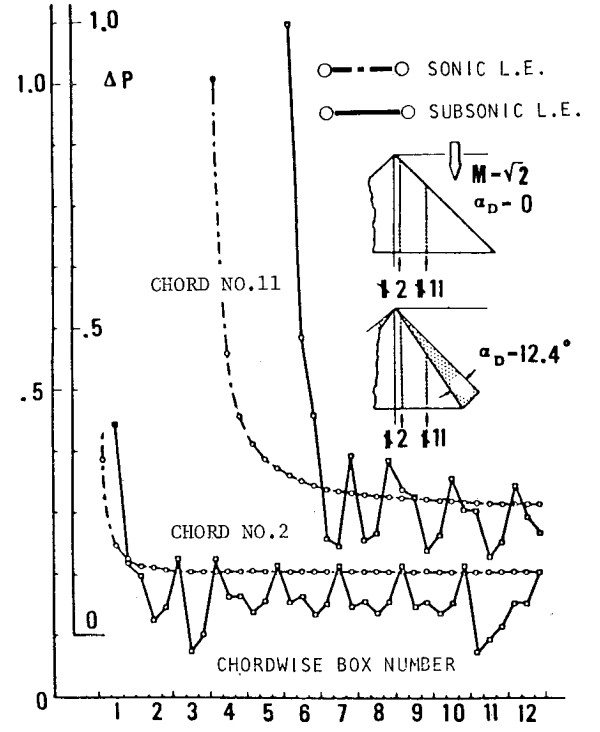

Fig. 2 Chordwise ΔP for sonic and subsonic wing leading edges.

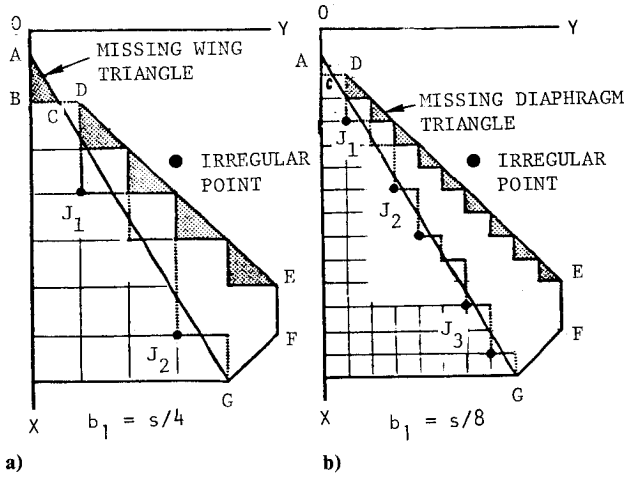

Fig. 3 Jagged leading edges due to discrete box grids.

Inherent Numerical Errors in Box Grid System

Since the wing planform in the numerical method is represented by a grid of boxes, the true wing leading edge is consequently replaced by a combination of jagged edges. Thus, the prima facie impression is that the inaccuracy is caused totally by the jagged leading edges to be replaced. This observation is not completely true. If the leading edge coincides with the Mach line, that is, the sonic leading edge, the leading edge is still jagged but is uniformly jagged. In this case, there exists no irregular point† in the wing leading edge. The chordwise pressure distributions along chords 2 and 11 are shown in Fig. 2. These pressure distributions exhibit smooth curves even though the leading edge is jagged but nonfluctuated as shown in Fig. 3a. However, if the leading edges become subsonic, there exist the irregular points of

†Irregular point is defined as the downstream corner of region where the leading edge cuts more than one box on the chordwise and spanwise strips.

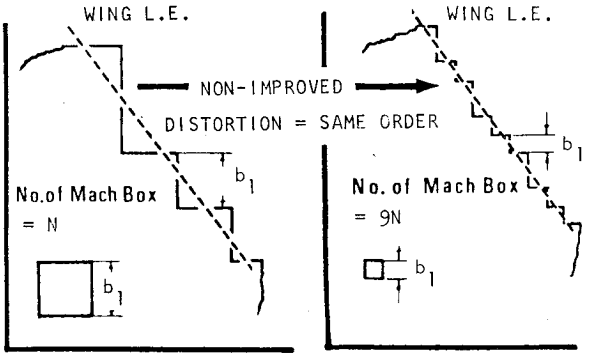

Fig. 4 Nonconvergent errors due to irregular points.

$J_1, J_2 \ldots$ as shown in Fig. 3. Then, the similar chordwise pressure distributions display widely fluctuated curves as shown in Fig. 2.

The previous studies[7] have revealed that these highly irregular pressure fluctuations are produced by:

1) Singular nature of AICs along the forward Mach cones emanating from the receiving points.

2) Strong upwash which is discontinuous and singular at a subsonic leading edge and is in the opposite direction on the diaphragm ahead of the leading edge.

3) Irregular points produced by the multibox jagged leading edge of a grid of boxes as illustrated in Fig. 3.

These effects combine to cause noticeable fluctuations in the velocity potential functions which when differentiated cause the pressure distribution to oscillate unrealistically chordwise and spanwise over the wing planform.

Converging and Nonconverging Errors

Errors Due to Missing Diaphragm Triangles

The missing areas, which are not counted in the Mach box grid system, are triangles along Mach lines emanating from the wing apex of the off-wing diaphragm. The other missing areas are triangles in the wing apex area as shown in Fig. 4. The missing wing triangles disappear for the nonswept rectangular wing. The box grid is now subdivided, and the box dimension in the original grid system is b_1 in the streamwise direction and b_1/N in the subdivided grid system; the ratio of this missing diaphragm area to the total diaphragm is reduced by approximately $1/N$. In the finer box grid system, these missing triangles lie close to the Mach line emanating from the wing apex as shown in Fig. 3b. The upwash on the wing diaphragm region is singular at the subsonic leading edge and vanishes at the wing apex Mach line. Therefore, the error caused by these missing diaphragm triangles can be reduced by applying the finer box grid system. This type of error is designated the converging error in this paper.

Errors Due to Missing Wing Triangles

Except for the nonswept rectangular wing, there always exist some missing areas which result from replacing the wing by a box grid system. If one subdivides the original one by b_1/N, this missing area is reduced by $1/N^2$. Thus, these are converging errors.

Errors Caused by Irregular Points

As discussed in the previous section, the leading edge which is not parallel to the Mach ray is represented by an irregular pattern of Mach boxes. In the box grid system, the minimum unit scale is represented by a dimension such as one of the sides of the box. If the box grid system is subdivided, the distortion of the jagged edge in comparison to the minimum unit scale of the box grid is not improved. There are also similar multijagged leading edge and irregular points which can not be decreased by applying the finer box grid system as shown in Fig. 4. Thus, the errors caused by irregular points are nonconverging errors.

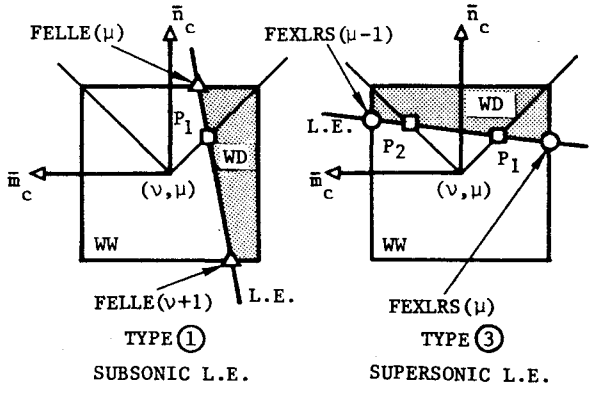

Fig. 5 Partitioned wing boxes of trapezoidal cut.

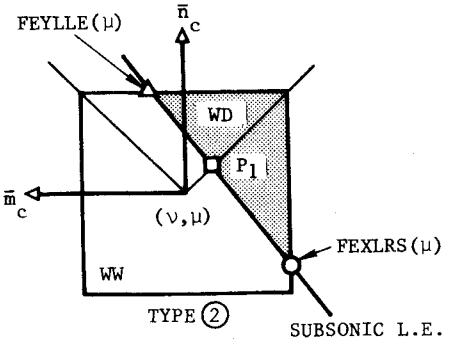

Fig. 6 Partitioned wing box of triangle cut.

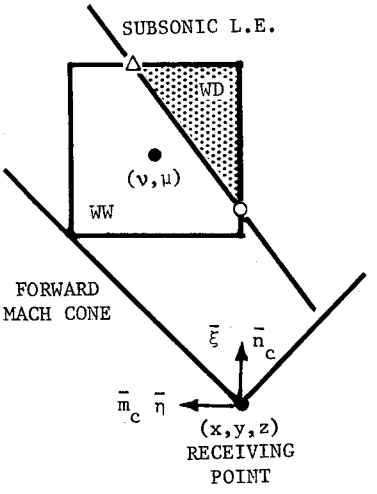

Fig. 7 Leading-edge box inside forward Mach cone.

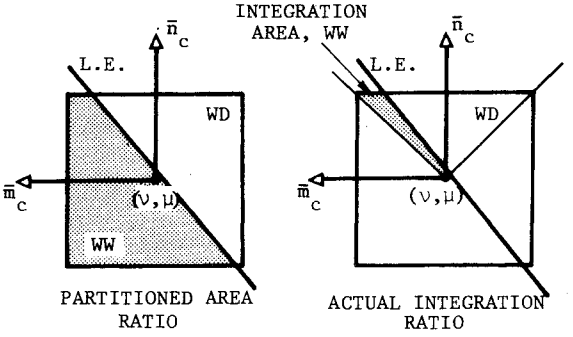

Fig. 8 Actual integration area for leading-edge wing box.

Errors Caused by Numerical Computation

In the numerical computation, the upwash over a unit box area is assumed to be uniform by providing a linear variation of the velocity potential functions. The errors caused by this assumption can be reduced by the finer box grid system and are converging ones.

Geometry of Leading Edge Boxes

The wing (or tail) leading edges intersect with sides of the wing (tail) leading-edge boxes. Therefore, the parameters necessary to integrate the AICs over the partitioned boxes are determined. The partitioned boxes are classified into three types by the way the subsonic or supersonic leading edge cuts them. These are the partitioned wing boxes of trapezoidal cut by both subsonic and supersonic leading edges as shown in Fig. 5. These are classified by Types 1 and 3, respectively. The box of triangle cut by the subsonic leading edge (on no occasion cut by the supersonic leading edge) is classified by Type 2 as shown in Fig. 6. The necessary parameters for these types are evaluated for both the leading-edge wing and diaphragm boxes. FELLE and FEXLRS are the intersection points between the wing leading edge and box sides in the $\bar{n}_c, \bar{m}_c$ coordinate system whose origin is at ν,μ.

The aerodynamic influence coefficient for a leading-edge box (ν,μ) can be computed by the limit integral of Eq. (6),

$$C_{\bar{\nu}\bar{\mu}\bar{\lambda}}{}^{\nu,\mu} = -\frac{1}{\pi}\int\int_{A(\nu,\mu)}\int [e^{-ik_1\xi}\cos(k_1 R_h/M)/R_h]\,ds$$

$$= -\frac{1}{\pi}\int\int_{WW(\nu,\mu)}\int [\ ]\,ds - \frac{1}{\pi}\int\int_{WD(\nu,\mu)}\int [\ ]\,ds$$

$$= C_{\bar{\nu}\bar{\mu}\bar{\lambda}}{}^{WW(\nu,\mu)} + C_{\bar{\nu}\bar{\mu}\bar{\lambda}}{}^{WD(\nu,\mu)} \qquad (10)$$

Receiving Point Outside the Sending Box

If the receiving point is outside the sending leading-edge box and is inside the forward Mach cone, as illustrated in Fig. 7, each integration area is approximately proportional to these partitioned areas. Also, the variation of the integrands in Eq. (10) is assumed to be small. Therefore, the following approximation is applied.

Box Inside of Forward Mach Cone

$$C_{\bar{\nu}\bar{\mu}\bar{\lambda}}{}^{WW(\nu,\mu)} \simeq WW(\nu,\mu)\,C_{\bar{\nu}\bar{\mu}\bar{\lambda}} \qquad (11)$$

$$C_{\bar{\nu}\bar{\mu}\bar{\lambda}}{}^{WD(\nu,\mu)} \simeq WD(\nu,\mu)\,C_{\bar{\nu}\bar{\mu}\bar{\lambda}} \qquad (12)$$

Box on Edge of Forward Mach Cone

If the receiving box is located on the edge of forward Mach cone, the following correction is made by eliminating half of the sending box area,

$$C_{\bar{\nu}\bar{\mu}\bar{\lambda}}{}^{WW(\nu\mu)} \simeq \tfrac{1}{2}WW(\nu\mu)\,C_{\bar{\nu}\bar{\mu}\bar{\lambda}} \qquad (13)$$

$$C_{\bar{\nu}\bar{\mu}\bar{\lambda}}{}^{WD(\nu\mu)} \simeq WD(\nu\mu)\,C_{\bar{\nu}\bar{\mu}\bar{\lambda}} \qquad (14)$$

where

$$\bar{\nu}=\bar{\mu} \text{ and } \bar{\lambda}=0$$

Receiving Point Inside the Sending Box

When the sending and receiving boxes are coincident, the ratio of WW and WD (or DW and DD) is completely different from the ratio of the actual integration area as shown in Fig. 8. Also, the variation of the integrand in Eq. (10) is large. In this case, the actual integration is performed over each area. The integration over these wing and diaphragm portions can be obtained from Eqs. (7-9). For the leading-edge diaphragm box, the integration is required for computing a Type 1 box only.

For $k=0$, the exact integral can be derived. For example, the AIC for the leading-edge wing box of Type 1, as shown in

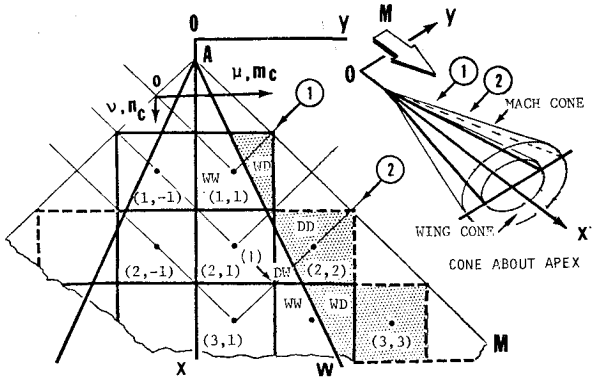

Fig. 9 Subsonic leading-edge wing and conical flow over diaphragm.

Fig. 5, is calculated by

$$COWD = -\frac{1}{\pi}[0.5\sin^{-1}(A+2B) - P_1\sin^{-1}(A+B/P_1)] - B/[\pi(1-\pi^2)^{1/2}][\ln|\{(1-A^2)1-A^2-4AB-4B^2\}^{1/2} + (1-A^2)]/B-2A| - \ln|2P_1\{[(1-A^2)1-A^2 - (2AB/P_1)-B^2/P_1^2]^{1/2} + (1-A^2)\}/B-2A|] - (0.5-P_1)/2 \quad (15)$$

$$COWW = C_{00} - COWD \quad (16)$$

where

$$P_1 = P_1(\hat{n}_c) \quad (17)$$

Similarly, the cases of Types 2 and 3 can be integrated.[4] For the unsteady case, $k \neq 0$, the integration is numerically evaluated.

Refined AIC Partition Scheme

The area partition scheme was first applied by Andrew and Moore[4] based on simple area weighted upwash. It was further developed by Chipman[8] by considering both wing and diaphragm upwash contributions. In the present work, the concept of area partition is motivated mainly by the need to minimize the influence of the irregular points which cause nonconverging errors.

The leading-edge wing boxes (1,1) and (2,1) and the diaphragm box (2,2) are partitioned by the wing leading edge as shown in Fig. 9. Therefore, the velocity potential is computed by

Box (1,1):

$$\Delta\phi(1,1) = \underbrace{COWWw(1,1)}_{\text{Wing contribution}} + \underbrace{COWDw(1,1)^{WD}}_{\text{Diaphragm contribution}} \quad (18)$$

where

$w(1,1)$ = modal normal wash at box center (1,1)

$w(1,1)^{WD}$ = normal wash on diaphragm portion WD which is determined by the conical flow concept

Box (2,1):

$$\Delta\phi(2,1) = \underbrace{COWWw(2,1) + (C_{10} \pm C_{11}/2)WW(1,1)w(1,1)}_{\text{Wing contribution}} + \underbrace{(C_{10} \pm C_{11}/2)WD(1,1)w(1,1)^{WD} + COWDw(2,1)^{WD}}_{\text{Diaphragm contribution}} \quad (19)$$

where $(\pm)$ indicate symmetry and antisymmetry modes.

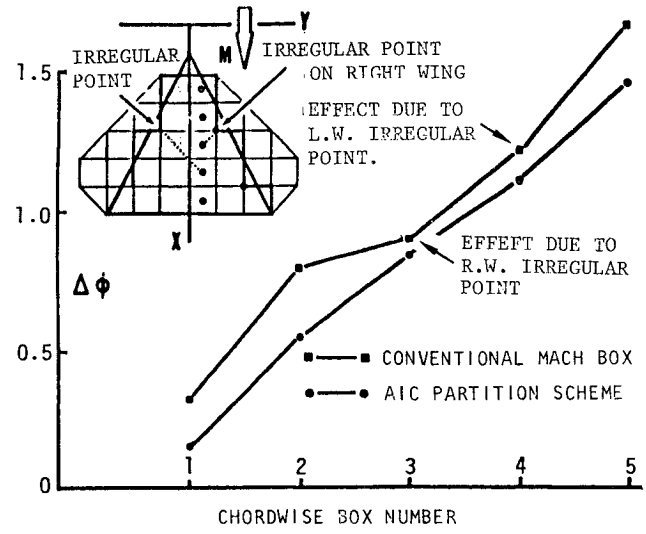

Fig. 10 Velocity potentials along chord 1.

Similarly, the AIC partition scheme will calculate $\Delta\phi(3,1)$ which consists of both wing and diaphragm contributions.

In the conventional Mach box scheme, the contribution from the normal washes on diaphragm boxes first appears at the irregular box (3,1).‡ However, in the AIC partition scheme, the diaphragm contribution appears in each step of computation at box (1,1) and box (2,1), etc. as shown in Eqs. (18) and (19). Thus, the irregularity of box (3,1) can now be minimized. The process of this computation may continue to the last leading-edge planform box on the wing tip.

Figure 10 illustrates the velocity potential functions along chord 1 computed from both the conventional and AIC partition schemes. The fluctuation caused by the irregular box (3,1) is now corrected and also that caused by the irregular box on the left wing is minimized.

Determination of the normal wash on the minor portion§ of the wing leading-edge box such as $w(1,1)^{WD}, w(2,2)^{DW}$ will be discussed in the following section.

Refined Normal Wash Computation

The normal washes on an apex box (1,1) in Fig. 9 are determined as follows:

Normal Wash on Wing Portion

This is determined by the modal deflection method,

$$w(1,1) = N_{RUW}{}^{1,1} - N_{RLW}{}^{1,1} \quad (20)$$

where

$$N_{RUW}{}^{1,1} = Df_j{}^{1,1}/Dt$$

$$N_{RLW}{}^{1,1} = -Df_j{}^{1,1}/Dt$$

The normal wash on the diaphragm portion $w(1,1)^{WD}$ is determined by applying the conical flow concept. Strictly speaking, this concept is valid only in the case of steady flow. The concept, however, may be extended to unsteady oscillatory flow by assuming that it is still valid if the oscillatory amplitude is small.

Consider two cones about the apex of wing. One of these is Mach cone and another is a wing cone as illustrated in Fig. 9. Next, consider a layer between these two cones cut by the

‡The irregular box is defined as a box which locates the downstream corner along a Mach line emanating from the irregular point of the wing leading edge.

§The leading-edge wing box is defined as a box whose area of wing portion WW is larger than the area of diaphragm portion WD. The WD is called the minor portion.

leading-edge diaphragm. By crossing this layer along a diagonal of the first diaphragm box (2,2) as shown by ② in Fig. 9, the average normal wash along this line, $w(2,2)$, is equivalent to the one along the diagonal on the diaphragm portion WD of box (1,1) as illustrated by ①. Therefore,

$$w(1,1)^{WD} = w(2,2) = N_{RUW}{}^{2,2} - N_{RLW}{}^{2,2} \tag{21}$$

In general, the first leading-edge diaphragm box is not always located next to the first leading-edge wing box as shown in Fig. 11. In this case, as a result of the first iteration, the normal wash on the diaphragm portion of the leading-edge box is determined in the following equation:

$$w(\nu,\mu)^{WD} = w(\nu+1,\mu+1) = \cdots\cdots = w(\nu+n-1,\mu+n-1)$$
$$= -[CODW(\nu+n,\mu+n)\,w(\nu+n,\mu+n-1)$$
$$+ \frac{1}{2}\sum_{i=0}^{n-1} C_{(n-i),(n-i)}\,W(i)\,]\Big/[CODD(\nu+n,\mu+n)$$
$$+ \sum_{i=0}^{n-1} C_{(n-i)(n-i)}\,WD(\nu+i,\mu+i)\,] \tag{22}$$

where

$$W(i) = WW(\nu+i,\mu+i)\,w(\nu+i,\mu+i)$$

Normal Wash on Minor Portion (Principle of Shifting Normal Wash in the Same Row)

The normal wash on the wing portion DW of a leading-edge diaphragm box in which $DW<DD$, can be determined from the value on the left wing box or,

$$w(\nu,\mu)^{DW} = w(\nu,\mu-1) \tag{23}$$

Similarly, the normal wash on the diaphragm portion WD or a leading-edge wing box can be determined from the value on the right diaphragm box, or

$$w(\nu,\mu)^{WD} = w(\nu,\mu+1) \tag{24}$$

Thus, the normal wash on the minor portion of the leading-edge box is obtained from the adjoining box on the same row. This is called the principle of shifting normal wash on the same row. The normal wash on the wing tip box, however, cannot be determined by the above principle. This is determined from the box on the Mach line emanating from the center of this box.[13]

From the foregoing procedure, the normal wash on both major and miinor portions of the leading-edge box can be determined. Then, the effective normal wash on the leading-edge box is an average value weighted by both areas. The normal wash on the leading-edge wing box, for example is

$$\bar{w}(\nu,\mu) = WW(\nu,\mu)\,w(\nu,\mu) + WD(\nu,\mu)\,w(\nu,\mu+1) \tag{25}$$

or for the first wing leading-edge box, it is

$$\bar{w}(\nu,\mu) = WW(\nu,\mu)\,w(\nu,\mu) + WD(\nu,\mu)\,w(\nu,\mu)^{WD} \tag{26}$$

Thus, the value of normal wash on either leading-edge wing or diaphragm box is a modified value and does not have the same value at the center of the box as the conventional numerical scheme indicates.

This computation scheme is extended to the three-dimensional interaction case such as a wing with dihedral and a wing-tail combination with a minor modification.[13]

Pressure Distribution and Generalized Forces

Once the refined velocity potential is evaluated over a lifting surface, the pressure distribution for the jth mode is found directly by

$$\Delta\bar{C}_{pj}{}^{n,m} = \frac{\Delta\bar{p}_j}{q} = \frac{2}{\alpha^{n,m} b_1 \beta}\left[\Delta\bar{\phi}_j(x,y)\,\Big|_{x_{LE}}^{x_{TE}} + i\alpha^{n,m} k_1 \Delta\bar{\phi}_j{}^{n,m}\right] \tag{27}$$

where $\alpha^{n,m}$ = area factor of box (n,m), which is used to adjust the basic box area along planform edges to compute the correct pressure value. For interior boxes, $\alpha^{n,m}$ is always unity.

The presence of the differentiation with respect to x in the pressure expression makes it preferable to calculate the generalized forces directly from the velocity potential, rather than by integration of the pressure distributions weighted by the various modal functions.

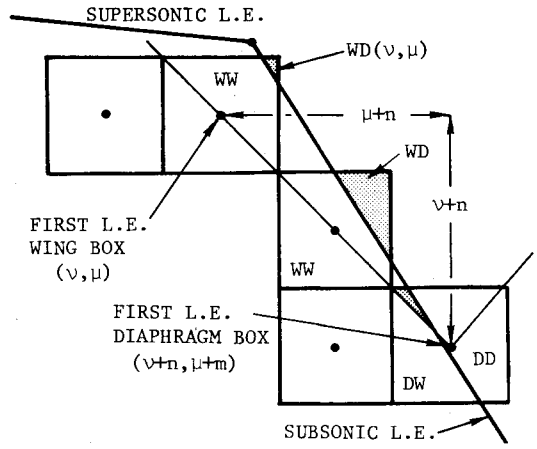

Fig. 11 First leading-edge wing and diaphragm boxes in general.

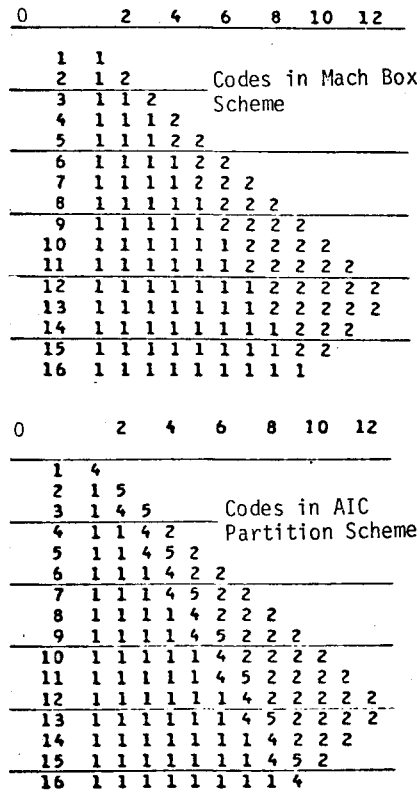

Fig. 12 Delta wing in computer code, $M = 1.414$.

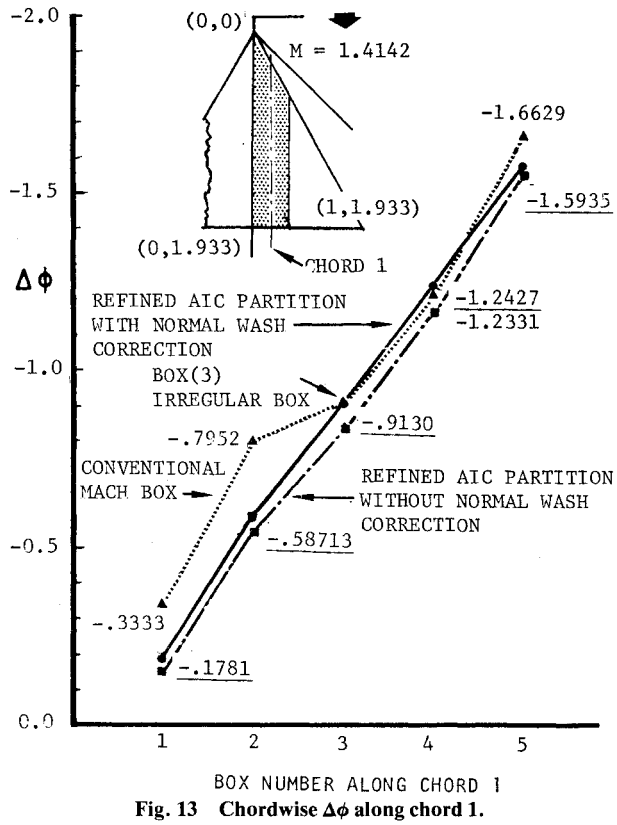

Fig. 13 Chordwise $\Delta\phi$ along chord 1.

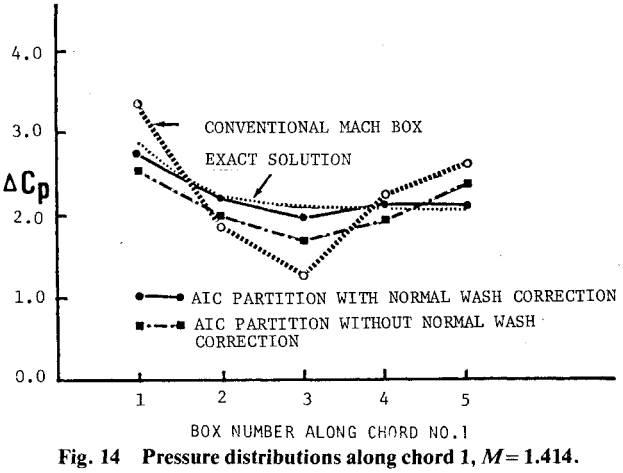

Fig. 14 Pressure distributions along chord 1, $M = 1.414$.

If $f_i(x,y)$ is the ith modal deflection in the nondimensional form, the generalized force associated with each box (n,m) due to the pressure for the jth mode is

$$\bar{Q}_{i_j}^{n,m} = \int\int_{A(n,m)} f_i(x,y)\,\Delta\bar{p}_j(x,y)\,dxdy \qquad (28)$$

Thus, once the refined velocity potential difference is obtained by applying the AIC partition scheme, the total generalized force in the ith mode due to unit generalized deflection of the jth mode is thus an algebraic summation over the boxes on either wing or tail surface.

Numerical Examples

Numerical examples to demonstrate the effectiveness of the present AIC partition method are given. These include steady and unsteady load distributions and aerodynamic coefficients for an AGARD delta wing for the planar case (shown in Fig. 13) and a wing-tail combination for the nonplanar interaction case. The leading edges of the wing-tail combination consist of the supersonic-subsonic multiedges. The applied Mach number is 1.414. Under these flowfields, the maps of the airfoil in the computing code are shown in Fig. 12. Compared to the conventional Mach box scheme, new box codes 4 and 5 are added. These are code 1, planform box; code 2, diaphragm box; code 3, wake box; code 4, leading-edge planform box; and code 5, leading edge diaphragm box.

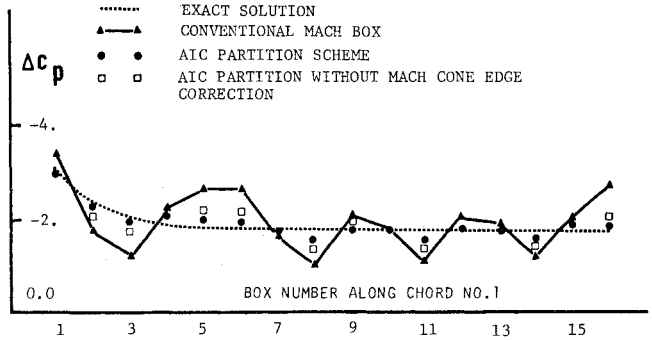

Fig. 15 Pressure distributions along chord 1 on delta wing with increased Mach boxes.

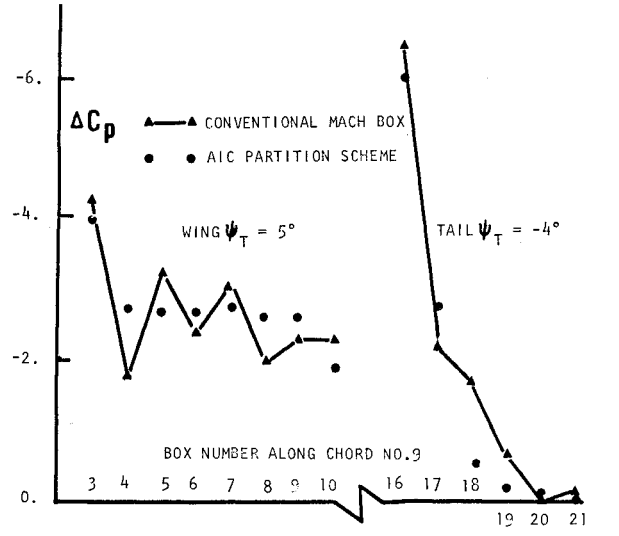

Fig. 16 Pressure distributions along chord 9 on a combination of wing-tail, $\Psi_W = 5$ deg, $\Psi_T = -4$ deg, $M = 1.562$, $k_f = 0$, pitch mode.

Steady Loads

Figure 13 shows the chordwise velocity potential functions along chord 1 of the delta wing for $M = 1.414$ and $k = 0$ with a pitch mode. The $\Delta\phi$ at box (3,1) is markedly fluctuated by the influence of the irregular point on the leading edge. Even with this coarse grid system, the velocity potential functions are remarkably improved by applying the AIC partition scheme. The similar velocity potential computed without normal wash correction on the diaphragm area is shown. The corresponding box pressure distributions are shown in Fig. 14. There is a substantial improvement by applying the AIC partition scheme with the normal wash correction.

Figure 15 shows the pressure distributions along chord 1 on the same delta wing. In this case, the number of boxes has been substantially increased. The pressure distribution without correction of the forward Mach cone edge expressed by Eq. (13) is also shown. From this figure, the above correction is essential.

An example of the three-dimensional interaction case is shown in Fig. 16. The pressure distributions along chord 9 are shown.

Unsteady Airloads and Aerodynamic Coefficients

The lifting surface tested for the unsteady case is the AGARD wing shown in Fig. 13. The tested Mach number is 1.414 and the reduced frequency based on the wing semispan, $k_s = 1.0$, which is equivalent to $k_l = 0.11111$. The oscillatory mode 1 is chosen as a pitching mode about the y axis whose origin is located at the wing apex; mode 2 is a plunging mode along the z axis.

The unsteady chordwise pressure distributions for oscillation in a pitch mode are shown in Figs. 17 and 18 for both conventional Mach box and refined AIC partition methods.

The chordwise pressure distributions along chord 1 for mode 2 are shown in Figs. 19 and 20. The real part of the chordwise pressure distributions computed by the conventional method does fluctuate unrealistically compared to the imaginary part of the pressure distribution. This is due to the fact that the normal washes due to the plunging mode are imaginary only on the lifting surface and are complex on the diaphragm region. Therefore, the influence of the irregular points deteriorates the velocity potential functions and results in the unrealistic pressure fluctuations.

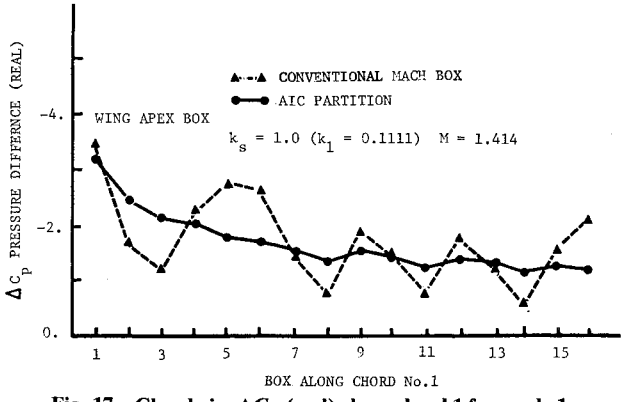

Fig. 17 Chordwise ΔC_P (real) along chord 1 for mode 1.

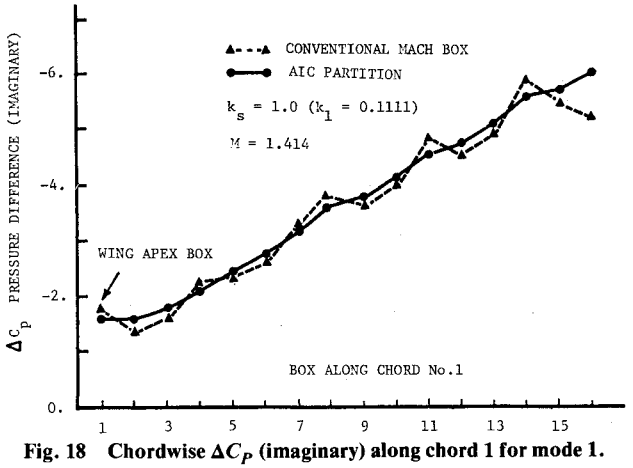

Fig. 18 Chordwise ΔC_P (imaginary) along chord 1 for mode 1.

Because of the lack of exact solutions to compare with these results, the index of accuracy is not directly available. A significant improvement to the anticipated pressure curves, however, can be detected in these figures from a practical point of view in that a gradual buildup of continuous curves can be expected for change to a lifting surface with a straight leading edge.

Integrated generalized forces are shown in Table 1. For the pitch-pitch mode, the generalized forces computed by the conventional method are acceptable. However, the generalized forces dominated by the plunging mode, computed by the conventional method, are no longer realistic and will result in a significant error in the dynamic response of the flying vehicle, as one can see from the pressure distributions in Fig. 19. Application of the conventional Mach box method for complex modes and high reduced-frequency cases would result in significant errors.[7,8]

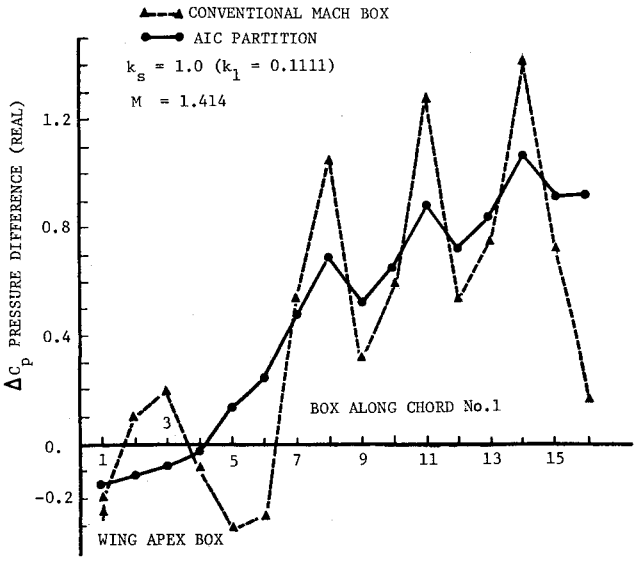

Fig. 19 Chordwise ΔC_P (real) along chord 1 for mode 2.

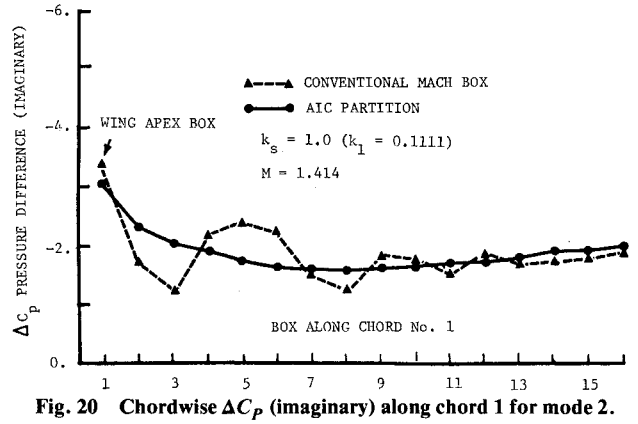

Fig. 20 Chordwise ΔC_P (imaginary) along chord 1 for mode 2.

Table 1 Generalized aerodynamic forces for AGARD wing ($M = 1.414$, $k_s = 1.0$)

Generalized forces	Mode 1 (pitch) Real	Mode 1 (pitch) Imaginary	Mode 2 (plunge) Real	Mode 2 (plunge) Imaginary
Mode 1				
Mach	−37.651094	−65.900715	1.6545599	−33.52104
AIC	−39.234225	−66.616592	1.0395314	−34.25425
Mode 2				
Mach	−23.708157	−37.866161	0.4955752	−21.03060
AIC	−24.419106	−38.107416	0.2523464	−21.37116

Mach = conventional Mach box; AIC = AIC partition scheme.

Conclusions

Theoretical studies to refine the predictions of unsteady aerodynamics of supersonic elastic aircraft have been made. Through these studies a theoretical interpretation of inaccuracies in the evaluation of airloads by application of the Mach box numerical scheme has been given. These inaccuracies are classified as either converging or nonconverging.

The improvement on the nonconverging errors, which are mainly caused by the influence of the irregular points on the planform leading edges, has been made by the AIC partition scheme. The AIC partition scheme exhibits a remarkable improvement even though a coarse box grid system is applied. The influence of the irregular points is not improved after a finer grid box system is applied. Thus, the pressure fluctuations are not completely eliminated with a finer box grid with the AIC partition scheme.

The increase in computer time involved in applying the AIC partition scheme is minor in comparison to the conventional scheme. Because of the few boxes located on the critical leading-edge area and of application of reusable AICs, the time increase is around the order of 5-8% depending upon Mach number, reduced frequency, geometry, and desired integration accuracy.

Because of theoretical ambiguity and elimination of the loading discontinuity on the multiedge wing, application of the velocity potential smoothing is not recommended in this refinement.

Demonstration on the nonplanar interaction case indicates a remarkable improvement. The previous refinements have not been designed to apply to these three-dimensional interaction cases.

Highly accurate values of load distributions, flutter stability boundaries, and dynamic response to continuous turbulence may now be obtained through an application of this method without excessive computing cost. It is felt that the method can contribute to the prediction of the dynamic behavior of supersonic flight vehicles.

Acknowledgment

This paper summarizes work performed under the Boeing Aerospace Company Independent Research & Development Program under B.F. Dotson, Military Aircraft Systems Division.

References

[1] Pines, S., Dujundji, J., and Neuringer, J., "Aerodynamic Flutter Derivatives for a Flexible Wing with Supersonic and Subsonic Edges," *Journal of Aeronautical Sciences,* Vol. 22, Oct. 1955, pp. 693-700.

[2] Zartarian, G. and Hsu, P.T., "Theoretical Studies on the Prediction of Unsteady Supersonic Airloads on Elastic Wings," *Investigations on the Use of Oscillatory Supersonic Aerodynamic Influence Coefficients,* WADC TR 56-97, Part I, Dec. 1955.

[3] Zartarian, G., *Rules for Application of Oscillatory Supersonic Aerodynamic Influence Coefficients,* WADC TR 56-97, Part II, Feb. 1956.

[4] Andrew, L.V. and Moore, M.T., "Further Developments in Supersonic Aerodynamic Influence Coefficient Methods," *Proceedings of AIAA Symposium on Structural Dynamics and Aeroelasticity,* Aug. 1966, pp. 203-213.

[5] Zartarian, G., Hsu, P.T., and Voss, H.M., "Application of Numerical Integration Techniques to the Low-Aspect-Ratio Flutter Problem to Subsonic and Supersonic Flows," Aeroelastic and Structures Research Lab., MIT, Tech. Rept. 52-3, Oct. 1954.

[6] Stark, V.J.E., "Calculation of Aerodynamic Forces on Two Oscillating Finite Wings at Low Supersonic Mach Numbers," Saab Aircraft Co., TN 53, Feb. 1964.

[7] Ii, J.M., "A Refined Prediction Method for the Unsteady Aerodynamics of Supersonic Elastic Aircraft," *Journal of Aircraft,* Vol. 9, Jan. 1972, pp. 61-68.

[8] Chipman, R.R., "An Improved Mach Box Approach for Supersonic Oscillatory Pressures," *Journal of Aircraft,* Vol. 14, Sept. 1977, pp. 887-893.

[9] Ii, J.M., Borland, C.J., and Hogley, J.R., "Prediction of Unsteady Aerodynamic Loadings of Non-Planar Wings and Wing-Tail Configurations in Supersonic Flow," *Theoretical Development, Program Usage, and Application,* AFFDL TR-71-108, Part I, March 1972.

[10] Ii, J.M. and Rowe, W.S., "Unsteady Aerodynamics of Non-Planar Wings and Wing-Tail Configurations of Elastic Flight Vehicles in Supersonic Flight," *Journal of Aircraft,* Vol. 10, Jan. 1973, pp. 19-27.

[11] Garrick, I.E. and Rubinow, S.I., "Theoretical Study of Air Forces on an Oscillating or Steady Thin Wing in a Supersonic Main Stream," NACA Rept. 872, June 1947.

[12] Evvard, J.C., "Use of Source Distributions for Evaluating Theoretical Aerodynamics of Thin Finite Wings at Supersonic Speeds," NACA Rept. 951, 1949.

[13] Ii, J.M. and Graham, M.L., "Refined Mach Box Numerical Method by AIC Partition Scheme," The Boeing Aerospace Co., Doc. D180-20702-1, Feb. 1979.